Journal of Alloys and Compounds 872 (2021) 159584

Contents lists available at ScienceDirect

Journal of Alloys and Compounds

journal homepage: www.elsevier.com/locate/jalcom

The effect of graphene structural integrity on the power factor of tin selenide nanocomposite

Manal Alsalama[a,*], Hicham Hamoudi[b], Khaled M. Youssef[c]

[a] Department of Sustainable Development, Hamad Bin Khalifa University, Doha 5825, Qatar
[b] Qatar Environment and Energy Research Institute, Doha 34110, Qatar
[c] Department of Materials Science and Technology, Qatar University, Doha 2713, Qatar

ARTICLE INFO

Article history:
Received 24 January 2021
Received in revised form 15 March 2021
Accepted 17 March 2021
Available online 20 March 2021

Keywords:
Thermoelectric materials
Milling time
Tin selenide, Graphene
Composites
Power factor

ABSTRACT

Tin selenide graphene nanocomposites (SnSe/GNPs) were fabricated with high-energy ball milling and hot pressing by varying the milling time of graphene. The effect of ball milling time on the graphene integrity and the dispersion homogeneity was investigated and the consequential variation in electrical properties of SnSe/GNPs were analyzed. The evolution of graphene sheets during milling as well as the crystal structure of SnSe/GNPs nanocomposites were systematically studied by X-ray diffraction, Raman analysis, scanning electron microscopy, and transmission electron microscopy. It has been proven that graphene was able to keep its crystallinity at short milling times, but it exhibits agglomeration and poor dispersion within the matrix. However, long milling time has a significant effect on increasing the disorders on graphene structure while it provides well dispersion of graphene. The calculated power factor increases with the addition of graphene and with increasing graphene milling time. The increased power factor is attributed to the homogeneous distribution of graphene, which results in a significant increase in electrical conductivity. At 773 K, the lowest power factor value was reported for the 1-min graphene-milled sample, whereas a 40% enhancement was reported for the 2-h graphene-milled sample. Across a wide temperature range (298–720 K), the 12-h graphene-milled sample shows the best performance owing to the simultaneous increase of electrical conductivity and Seebeck coefficient. These findings indicate the positive effect of milling time on the distribution of graphene, which in turn enables graphene to form a continuous net for carriers to move. This study could provide a greater understanding of the control factors of the mechanical milling process for preparing SnSe/GNPs nanocomposites in order to take full advantage of graphene's extraordinary properties by improving its distribution within the tin-selenide- based composite.

1. Introduction

Thermoelectric materials are attracting significant research interest as they offer a viable route to generate power from the massive amount of wasted heat resources such as in the automobile manufacturing industry and intensive industrial operations. Among several thermoelectric materials, layered single-crystal tin selenide (SnSe) has gained significant interest as a promising material for mid- to high-temperature thermoelectric applications [1]. However, SnSe in its single-crystal form is not suitable for practical applications because of the high cost of production, weak cleaving properties, and highly anisotropic thermoelectric properties [2,3]. Therefore, as polycrystalline SnSe exhibits better mechanical properties under easily controlled production conditions, it could be a feasible alternative candidate. However, compared with its single-crystal form, polycrystalline SnSe samples possess higher thermal conductivity and lower carrier mobility [4,5]. Therefore, much attention has been paid to the optimization of polycrystalline SnSe to improve its thermoelectric performance [6–9]. Among several approaches that have been investigated, compositing by incorporating external additive material into the SnSe matrix is considered to be a promising strategy [10–13]. The role of the additive materials in enhancing the thermoelectric performance of the thermoelectric composite is threefold. First, the additive material can improve electrical conductivity by increasing the carrier concentration and/or the carrier mobility. Second, it can improve the Seebeck coefficient by introducing interfaces with the matrix where low-energy charge carriers can be filtered. Third, the additive materials produce high-density interfaces with the matrix that suppress the thermal conductivity via phonon scattering. For example, Li et al. [11] reported a

* Corresponding author.
E-mail address: mmalsalama@hbku.edu.qa (M. Alsalama).

https://doi.org/10.1016/j.jallcom.2021.159584
0925-8388/

ZT of 1.26 at 886 K for SnSe/1.5 vol% PbTe composite due to the increase in the power factor (PF) and reduction of the thermal conductivity. The increase in PF was attributed to the enhanced electrical conductivity by increasing the carrier concentration. Another study [12] reported an approximately 69% increase in PF owing to the enhancement of electrical conductivity when 2.5 vol% of carbon black nanoinclusions were embedded into the SnSe matrix. Ju et al. [10] found that the introduction of 1 wt% of SiC into the SnSe matrix enhanced the ZT value. The embedded SiC nanoinclusions produced numerous interfaces within the matrix that acted as phonon-scattering centers, thus reducing thermal conductivity. In addition, these nanoinclusions served as filtering centers where high-energy carriers only could pass through, thereby leading to an increase in the Seebeck coefficient.

Graphene, a two-dimensional (2D) material with a high specific area, is a promising additive material in the field of thermoelectrics due to its extraordinary electrical, thermal, and mechanical properties [14,15]. In the last few years, graphene has been incorporated into several thermoelectric systems [3,15–25]. However, researchers encountered several challenges that reduced the effectiveness of graphene in improving thermoelectric properties. For instance, the agglomeration of graphene during processing caused poor dispersion and weak interface bonding, limiting its functionality in improving the composites' thermoelectric properties [15,19–21,26,27]. It was found that a large 2D surface area, along with the flexible characteristics of graphene, led to significant difficulty in achieving uniform distribution within the matrix. Tang et al. [28] found that carrier mobility decreased with increasing graphene content in the $Cu_{1.8}S$ matrix as a result of the poor dispersion and agglomeration of graphene. Similarly, Feng et al. [21] observed better thermoelectric performance of the $CoSb_3$-graphene composites prepared by the in-situ solvothermal process than that prepared by grinding. Even though the same amount of graphene was used in both techniques, the authors attributed this decrease in the performance of the samples prepared by grinding to the agglomeration of graphene into thick flakes.

Ball milling has been widely used to successfully prepare composites with good graphene dispersion [27,29] The shear forces from the milling process and ball collisions help to exfoliate the graphene sheets and prevent their agglomeration. Despite evidence that ball milling would enhance the distribution of graphene, there is a lack of information in the literature about the effects of these shear forces and the severe plastic deformation during milling on the structural integrity of graphene in thermoelectric materials. The high shear forces with longer milling times might increase fragmentation, plastic deformation, defects, and disordering in graphene, which in turn could influence the overall PF values. Therefore, the present study synthesized and examined the nanostructure of several SnSe/graphene nanocomposites produced by ball milling and hot-pressing techniques. In particular, this study focuses on the influence of milling time on the graphene structure in the SnSe matrix and its corresponding effect on PF values.

2. Experimental

Nominal compositions of SnSe and SnSe/0.5 wt% GNP samples were prepared from elemental powders of Sn (Alfa Aesar, 99.995% purity, and −325 mesh), Se (Alfa Aesar, 99.999% purity, −100 mesh), and GNPs (Sigma-Aldrich). The powders were loaded and sealed in a stainless steel vial under an ultra-high-purity argon atmosphere (O_2 < 0.5 ppm) with a ball-to-powder ratio of 10:1 and milled for a total of 12 h. The milling process was carried out in a SPEX 8000 high-energy mill at room temperature. To investigate the effect of milling on the structural integrity of GNP, the 0.5 wt% GNPs were added to different batches of the SnSe at various milling time intervals (at the beginning of ball milling, 12 h; at the last 2 h; at the last 1 h; at the last 10 min; and at the last 1 min). Table 1 shows the milling conditions of these samples and the corresponding sample notation that is used throughout this study. Consolidation of the milled powders was carried out using hot pressing under an ultra-high-purity argon atmosphere. The hot compaction was performed at 773 K for 10 min under a uniaxial applied pressure of 1 GPa. The consolidated samples were in the form of discs measuring 12.7 mm diameter and 3 mm thickness.

Table 1
The notation of the prepared samples according to the graphene addition time during milling.

Sample notation	GNPs addition time
GNP-12 h	At the beginning of milling (12 h)
GNP-2 h	At the last 2 h
GNP-1 h	At the last 1 h
GNP-10 m	At the last 10 min
GNP-1 m	At the last 1 min
Pristine SnSe	—

X-ray diffraction (XRD) was performed on the processed samples using an Empyrean diffractometer (Malvern Panalytica, Ltd., Malvern, United Kingdom) with CuK_a (λ = 0.1542 nm) radiation. The XRD analyses were carried out at 45 kV, 40 mA, and 25 °C with a scanning range from 20° to 70°, a step size of 0.013°, and a scan rate of 0.044° s^{-1}. The morphology and the structural characteristics of the milled powders were investigated using a scanning electron microscope (SEM; Nano Nova 450; FEI Company, Hillsboro, Oregon, USA). Two transmission electron microscope (TEM) devices were used to investigate the microstructure and the element distribution in the processed samples (TECANI G2 field emission gun TEM; FEI Company). The samples were prepared by dispersing a small amount of the powder sample and sonicating it in isopropyl alcohol in an ultra sonicator bath for 10–20 min. Then, using a micropipette, 10 μL of the dispersed solution was taken and drop-casted onto the carbon film copper grid of 300 mesh. When the mesh dried, it was taken to the microscope for imaging. The other device is the field emission gun TALOS (FEI Company, Hillsboro, Oregon, USA), which was equipped with a high-angle annular dark-field (HAADF) detector and an energy-dispersive X-ray detector (FEI Company) and operated at 200 kV. Esprit software from Bruker (Billerica, Massachusetts, USA) was used to obtain qualitative element analyses. The cross-sectional TEM lamella was prepared using the Versa 3D DualBeam focused ion beam SEM (FEI Company). The thickness of the TEM lamellas was between 25 and 75 nm. A DXR Raman imaging microscope (Thermo Fisher Scientific, Waltham, Massachusetts, USA) with a laser wavelength of 532 nm was used to examine the structural integrity of the GNPs in the milled samples at different time intervals.

For the PF measurements, the Seebeck coefficient and the electrical conductivity of the consolidated samples were measured simultaneously using the SBA 458 Nemesis (NETZSCH-Gerätebau GmbH, Selb, Germany). These measurements were performed on the samples from room temperature to 773 K under an ultra-high-purity argon atmosphere. The measurements were repeated at least three times for each sample. The Hall coefficient (R_H) experiments were carried out using a calibrated Model 8404 Hall effect measurement system (Lake Shore Cryotronics, Inc., Westerville, Ohio, USA) at room temperature under air using a Differential Scanning Calorimetry (DSC) magnetic field of 1 Tesla. The uncertainty for the experimental determination of the power factor is about 5–11% for all samples.

3. Results and discussion

The XRD patterns for the pristine SnSe, as-received GNP and the SnSe composites in which the GNPs were added at different milling times are shown in Fig. 1. The XRD peaks of all the as- milled samples were indexed to the orthorhombic SnSe phase with space group

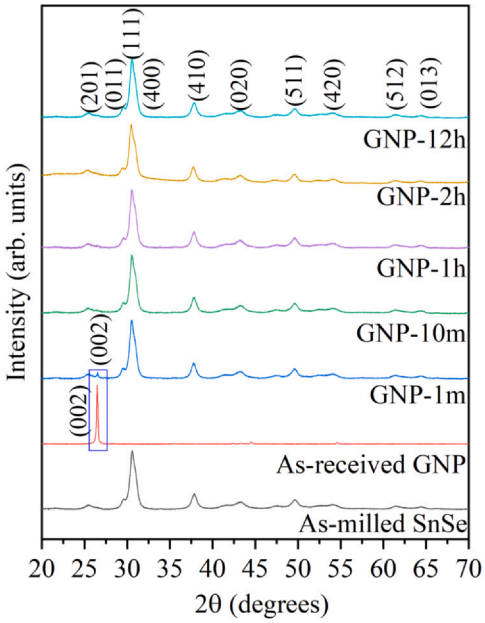

Fig. 1. XRD for the pristine SnSe, the as-received GNP, and the SnSe/GNPs composites at different graphene milling times. The (002) plane peak of the as-received GNP with the matched (002) plane peak in the GNP-1 m sample is circled.

Pmna (JCPDS card number 48-1224). No extra peaks for a second phase or contamination from the milling process were detected. The broadening of the peaks indicates the refinement of the grain size. This was analyzed by estimating the grain size using XRD data and the Warren- Averbach method [30].

$$\frac{\beta_{hkl}^2}{\tan^2\theta} = \frac{\lambda}{D}\left(\frac{\beta_{hkl}}{\tan\theta\sin\theta}\right) + 25(\varepsilon) \quad (1)$$

where $\beta_{hkl}$is the width of the peak at half-maximum intensity, λ is the wavelength of the x-ray beam, θ is the peak position, D is the average grain size, and ε is the lattice strain. Fitting $\beta_{hkl}{}^2/\tan^2\theta$ vs. $\beta_{hkl}/(\tan\theta\ \sin\theta)$ gave a linear regression fit of at least 0.7 for all measurements.

The calculated average grain size values for SnSe, GNP-1 m, GNP-10 m, GNP-1 h, GNP-2 h, and GNP-12 h were 10 nm, 9 nm, 11 nm, 9 nm, 11 nm, and 10 nm, respectively. TEM investigations were performed in order to confirm the grain size values obtained from the XRD analysis. Fig. 2 shows the dark-field, bright field image of the GNP-2 h sample and its corresponding selected area electron diffraction (SAED) pattern along with the statistical distribution of grain size. As presented, the average grain size is 14 nm, which confirms the reliability of XRD calculations. It is worth mentioning that the signature (002) peak of graphene was only shown in the XRD of the SnSe composite with GNP added at the last minute of milling (see Fig. 1). The appearance of the graphene (002) peak only in this composite sample could be attributed to the agglomeration of GNP at the short milling time (1 min). These results are in good agreement with the results obtained after milling the $Bi_{85}Sb_{15}$- 0.08%Gr composite [31]. However, the absence of graphene (002) peak in other composite samples may either attributed to the loss of graphene crystallinity with milling time [32] or to the low concentration of the distributed graphene that could not be detected by XRD [16].

To assess the structural evolution and integrity of graphene with increasing milling time, Raman analysis was conducted for the SnSe/GNPs composites. These Raman spectra were compared with that of the as-received GNPs (see Fig. 3). The spectra of all the samples exhibit the two typical G and 2D fingerprint peaks of crystalline carbon material. The G peak is the primary Raman active mode that is associated with the vibration of sp^2 bonded carbon atoms. It appears at around 1580 cm^{-1}. The 2D peak is another characteristic peak of the graphene structure. It appears at around 2700 cm^{-1}. The spectra also exhibit the two peaks of the defected carbon materials: the D peak, which is associated with the disorders in the lattice structure and appears at around 1350 cm^{-1}, and the D′ peaks, which represent the finite graphite crystals and graphene edges, and they appear at around 1620 cm^{-1} [2,20,33–36]. Table 2 illustrates the range of the Raman shift values of the as-received graphene as well as the powder composite samples and both the I_D/I_G and I_{2D}/I_G ratios. As revealed from the spectra of the as-received graphene, the D, G, and 2D peaks are narrow with high intensities. However, the 2D peak is much lower than the G peak, indicating that our starting graphene nanoplatelets have multiple layers [37,38]. It is worth mentioning that the GNP-1 m sample does not show any Raman peaks, even though we ran the test several times. However, the presence of graphene in this sample is confirmed by XRD. The absence of the corresponding peaks in Raman spectroscopy could be attributed to the agglomeration of graphene in this sample. After increasing the milling time from 10 min up to 12 h, it is obvious that the 2D peak is significantly weakened and broadened. The G peak was broadening as well due to the presence of the D′ peak. The D band gradually became the most prominent peak in the Raman spectra. This finding indicates that graphene crystallinity has been partially lost and there is a partial conversion of sp^2 carbon atoms to sp^3 hybridization by the induced disorders and defects due to milling [35,38,39]. The broadening of the D′ peak with increasing milling time shows the presence of extra graphene edges, which could represent extra fragmentations of the graphene sheets. As a consequence, the I_D/I_G ratio increases gradually with milling time from 0.26 for the as-received GNP to 0.362, 0.690, 0.945, and 1.441 for GNP-10, GNP-1 h, GNP-2 h, and GNP-12 h, respectively (see Table 2 and Fig. 3). These results show that a short milling time allows graphene to preserve its crystallinity the most. A long milling time led to fragmentation, defects, and disordering of the graphene's structure. Moreover, compared with the as-received GNPs, the intensity ratio of the I_{2D}/I_G first decreases from 0.552 to 0.5 after milling for 10 min, suggesting the existence of multiple graphene layers [40]. Then, the ratio increases to 0.61 and 0.65 with longer milling times (1 h and 2 h, respectively), suggesting that graphene exfoliates only a few layers [27,39]. After 12 h of milling, the I_{2D}/I_G ratio decreases to 0.27. Owing to the flexible nature of graphene and the weak Vander Waals forces between its layers, graphene undergoes severe plastic deformation and exhibits folding, bending, wrapping, and crumbling when exposed to high impact forces after 12 h of milling. This could lead to extra bending and folding of the graphene sheets in an effort to minimize the surface area and the dangling bonds that are created during milling. These extra folding of the graphene sheets could indicate a higher number of stacked graphene layers by Raman analysis, which results in the observed reduction in the I_{2D}/I_G ratio. These findings are in agreement with the previously reported Raman analysis for the effect of milling on the graphene structure [29,41–43]. However, the presence of all the characteristic peaks with significant intensities after up to 12 h of milling indicates that graphene is able to partially maintain its graphitic structure [44].

To further confirm the graphene integrity and its distribution in the SnSe/GNPs composite samples with milling time, SEM-EDS analysis has been performed. Fig. 4 shows the SEM-EDS images of the as-milled SnSe, GNP-1 m, and GNP-10 m composites. Fig. 4B shows the GNP-1 m sample in which graphene sheets were not identified except with small sheets at certain areas. This finding is in agreement with the XRD data and confirms the poor distribution of graphene within the sample. Fig. 4C shows GNP-10 m, in which large graphene sheets are observed in different areas, indicating that the graphene was able to maintain its structure during this short

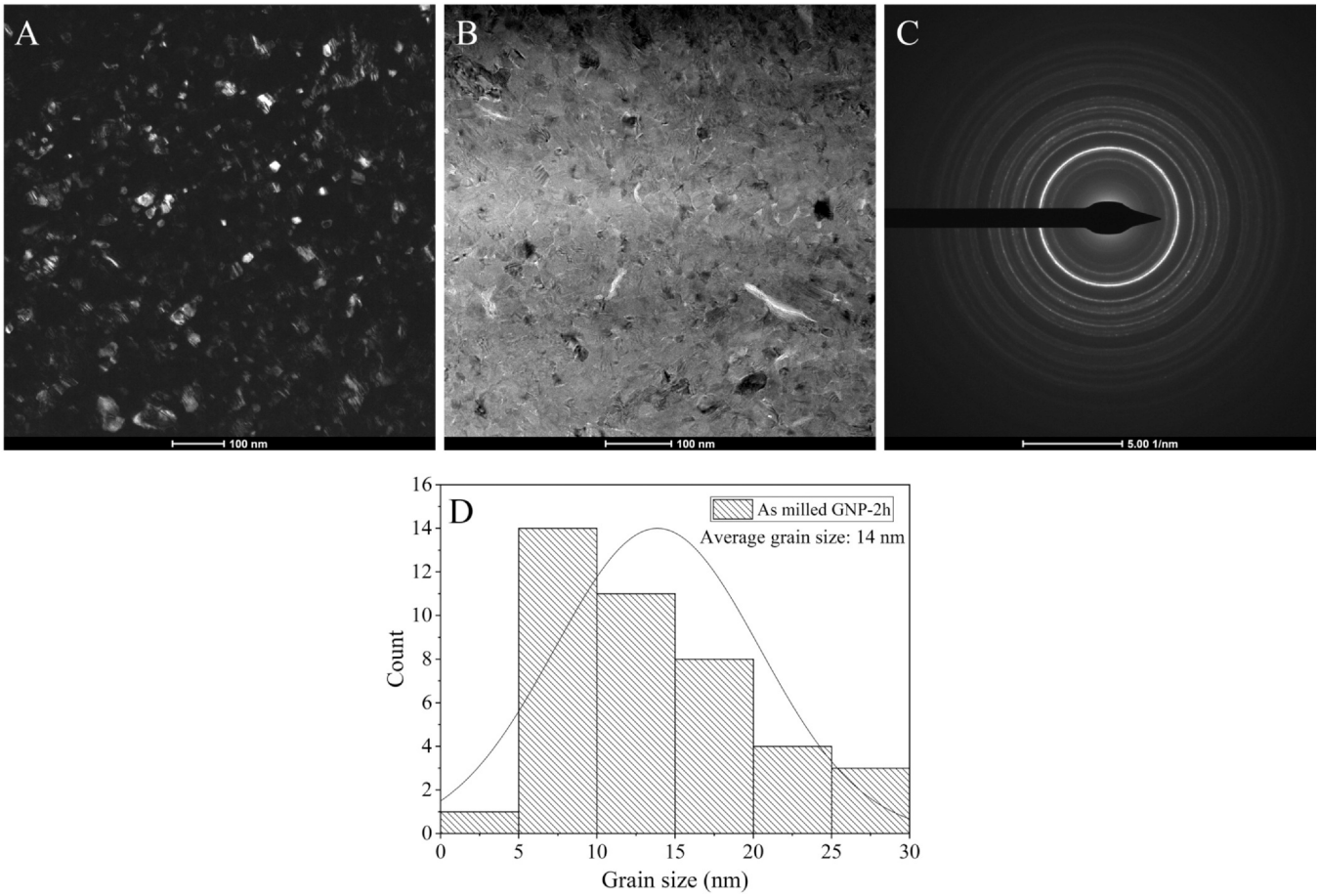

Fig. 2. (A) Dark-field image of the as-milled GNP-2 h sample, (B) Bright-field image of the as-milled GNP-2 h sample, (C) SAED pattern of the GNP-2 h sample, and (D) grain size distribution of the GNP-2 h sample.

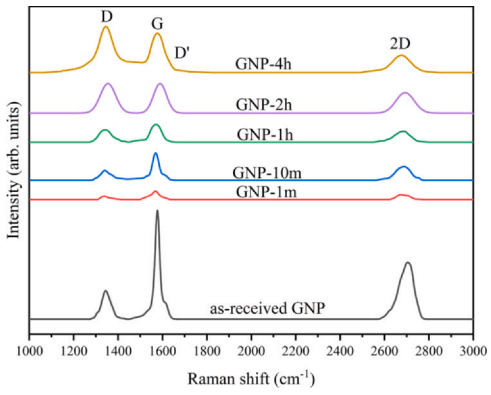

Fig. 3. Raman spectra of as-received graphene and as-milled SnSe/GNPs composites at different milling times.

Table 2
Raman data for as-received GNPs and graphene powder SnSe-GNPs composites milled at different times.

Sample	Raman Shift (cm^{-1})			Intensity Ratio	
	D	G	2D	I_D/I_G	I_{2D}/I_G
GNP-12 h	1348.9	1585.2	2685.4	1.441	0.27
GNP-2 h	1350	1580	2690	0.945	0.65
GNP-1 h	1342.2	1572.7	2685.4	0.690	0.61
GNP-10 m	1341.3	1570.8	2690.2	0.362	0.50
As-received GNPs	1346	1577.5	2706	0.260	0.522

milling time. This result agrees with the Raman data (Fig. 3). However, graphene sheets do not exhibit homogeneous distribution within the matrix, which may not support the continuous flow of carriers within the sample.

The Seebeck coefficient measurements for the pristine SnSe and SnSe/GNPs composite samples show monotonic behavior with positive values in the entire temperature range, indicating that SnSe and the composites are p-type and that holes are the majority carriers (see Fig. 5A). The behavior of the Seebeck coefficient with temperature for all samples is nonmonotonic. However, the Seebeck coefficient has a maximum value at a certain temperature (557–650 K) except for the pristine SnSe and GNP-12 h samples, which have maximum values at 300 K and 450 K, respectively. At temperatures higher than 650 K, the value of the Seebeck coefficient decreases, which could be attributed to the simultaneous excitation of minority carriers [17,45] and the high kinetic energy gained by the carriers. In turn, high kinetic energy enables the carriers to overcome the induced potential barriers at the interfaces [16,46], thus reducing the value of the Seebeck coefficient. From room temperature up to 700 K, only the GNP-12 h sample shows a higher Seebeck coefficient than the pristine sample. This finding could indicate that the increased graphene fragmentation with milling time produces extra interfaces between graphene and the matrix. These created interfaces could build potential barriers and act as scattering sites for the low-energy carriers [46–49].

The temperature dependence of electrical conductivity (σ) is shown in Fig. 5B. As can be seen, a gradual increase of σ with increasing the temperature is observed for all samples indicating semiconductor behavior for SnSe/GNPs composites [3,50]. It is

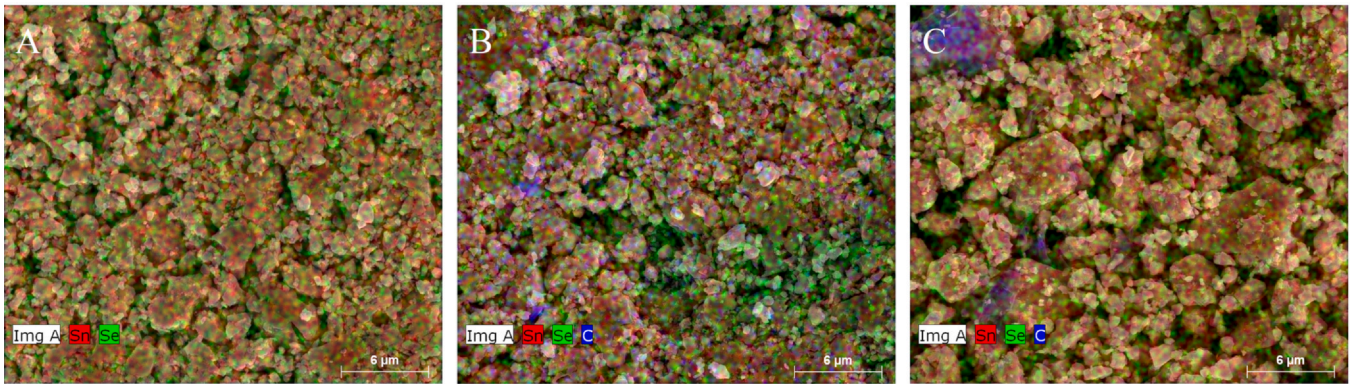

Fig. 4. SEM-EDS images of the as-milled powder of (A) pristine SnSe, (B) GNP-1 m sample, and (C) GNP-10 m sample.

noteworthy that the electrical conductivity of the SnSe/GNPs composite increases upon the introduction of conductive graphene nanoplatelets [3,15–17,19,45,50,51]. With increasing milling time, electrical conductivity increases gradually from 20 S/cm for the GNP-1 m sample to 34 S/cm for the GNP-2 h sample, and then it decreases slightly to 28 S/cm for the GNP-12 h sample at 773 K. As all SnSe/GNPs composite samples are prepared under similar preparation conditions and are embedded with the same graphene content (0.5 wt%), the only factor that affects the electrical conductivity is the structural integrity and distribution of graphene, which is varied with different milling times.

To further understand the electronic behavior of the pristine SnSe and SnSe/GNPs composite samples, Hall-effect measurements were performed. The carrier concentration (n) and carrier mobility (μ) were calculated from the formula $n = 1/(eR_H)$ and $\mu = \sigma R_H$, where e and σ are the electron charge and the electrical conductivity, respectively, and R_H is the Hall coefficient. The measured values are presented in Fig. 5D. The carrier concentration for the SnSe/GNPs composites with different milling times decreases compared with the pristine SnSe sample by several orders of magnitude. The higher carrier concentration of the GNP-10 m sample than that of the GNP-1 m sample could be related to the enhanced distribution of graphene in the GNP-10 m sample. The gradual reduction of carrier concentration with milling time could be attributed to the aggregation of graphene and the increased scattering of low-energy carriers at the boundaries and interfaces [16]. In contrast, carrier mobility increases with the addition of graphene and shows an increasing trend with the milling time by two to five orders of

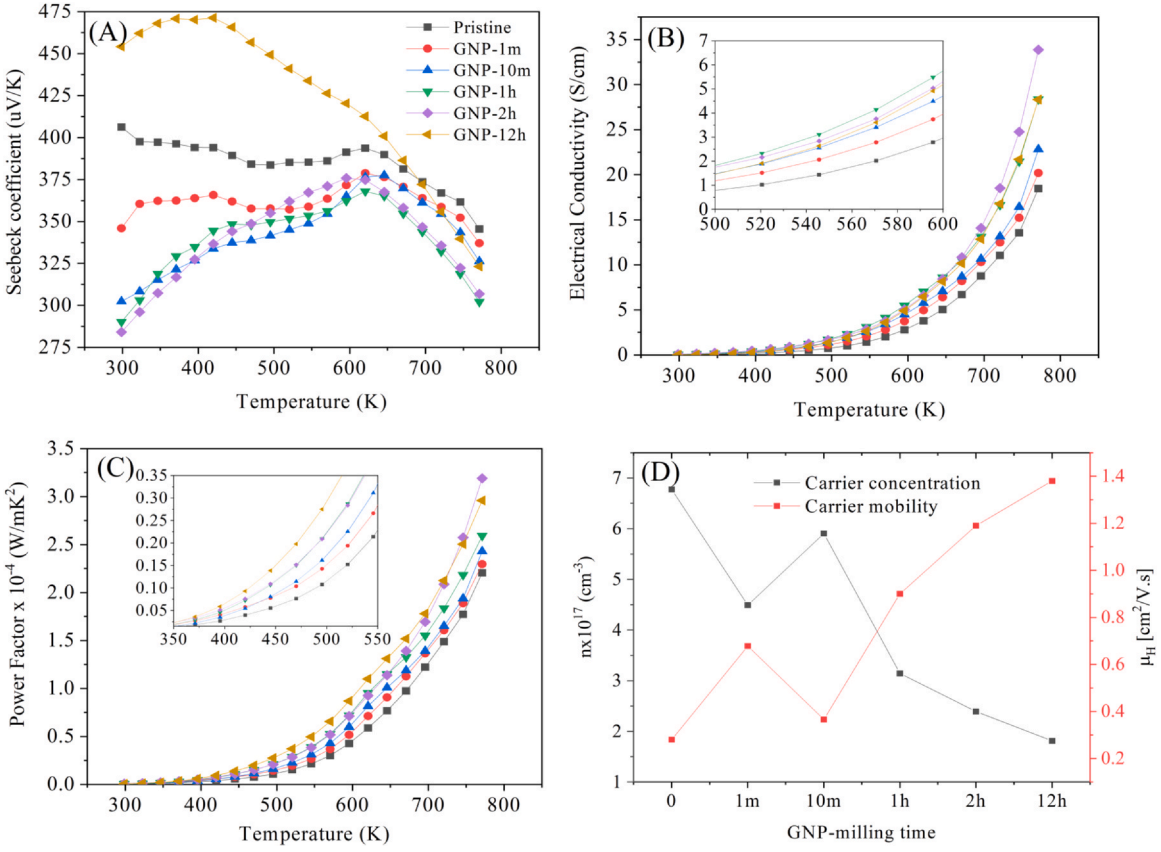

Fig. 5. Temperature dependence of (A) Seebeck coefficient, (B) electrical conductivity, (C) power factor, and (D) carrier's concentration and carrier's mobility of the pristine SnSe and SnSe/GNP composites as a function of the graphene milling time at room temperature.

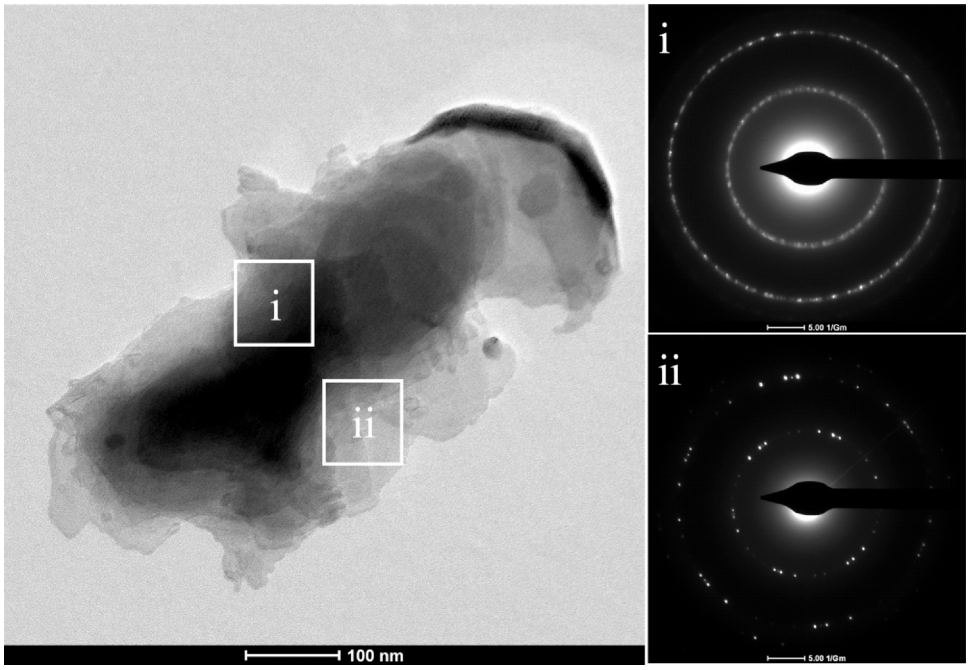

Fig. 6. A bright-field TEM image of the GNP-1 m sample with its corresponding SAED from two distinguished areas: (i) an area several layers thick and (ii) an area with a thickness of just a few layers. The GNP sheets appear to be agglomerated.

magnitude. The reduction in mobility for the GNP-10 m sample is accompanied by an increase in the carrier concentration, as shown in Fig. 5D.

The overall PF is calculated for all samples and presented in Fig. 5C. The PF values increase exponentially with increasing the temperature. All the SnSe composite samples showed higher PF values than that of pristine SnSe. However, among all samples, the maximum PF was 3.19×10^{-4} $wm^{-1}k^{-2}$ for the GNP-2 h sample at 773 K because it demonstrated the highest electrical conductivity of all the samples. However, the GNP-12 h sample exhibits the highest PF value in a wider temperature range (from room temperature up to 720 K) with a maximum PF value of 2.96×10^{-4} $wm^{-1}k^{-2}$ at 773 K. These PF values for both the GNP-2 h and GNP-12 h samples are higher than the values reported for the SnSe/GNPs composite (2.3×10^{-4} $wm^{-1}k^{-2}$), which is prepared by grinding with a similar amount (0.5 wt%) of graphene [3]. Because the increase in PF is a tradeoff between the homogeneous distribution of graphene and the preserved graphene integrity, it could be beneficial to have a partial deformed graphene structure for the sake of homogeneous distribution and to have extra interfaces in order to achieve good electrical transport properties.

In general, there is an inverse relationship between the Seebeck coefficient and electrical conductivity as both parameters interact inversely through carrier concentration. Interestingly, the GNP-12 h sample exhibits a higher Seebeck coefficient accompanied by higher electrical conductivity than the other SnSe/GNPs composites. This sample did not follow the trend of an inverse relationship between the Seebeck coefficient and the electrical conductivity in the temperature range of 298–700 K. This finding can be plausibly explained by the two equations that relate the Seebeck coefficient and electrical conductivity to the carrier concentration. The inverse relationship between the carrier concentration and the Seebeck coefficient is described by [52]:

$$S = \frac{8\pi^2 k_\beta^2}{3eh^2} m^* T \left(\frac{\pi}{3n}\right)^{2/3} \quad (2)$$

where e is the charge of the carrier, k_β is the Boltzmann constant, h is Plank's constant, and m* is the effective mass of the charge carrier. In contrast, the direct relationship between the electrical conductivity and both carrier concentration and carrier mobility is depicted in the following equation [52]:

$$\sigma = en\mu \quad (3)$$

As can be seen from Eq. (2), the maximum Seebeck coefficient is obtained when the carrier concentration is the lowest. Therefore, the high Seebeck coefficient for the GNP-12 h sample could be explained by the low carrier concentration (see Fig. 5D) that emerged after filtering the low-energy carriers at the SnSe-GNPs interfaces [15,18,28,31]. Eq. (3) explains the increase in electrical conductivity by increasing the carrier mobility that compensates for the reduction in carrier concentration and contributes significantly to the rise of the electrical conductivity for the GNP-12 h sample. It can be concluded that the enhanced distribution of graphene in the SnSe matrix plays a significant role in decoupling the relationship between the Seebeck coefficient and the electrical conductivity by decreasing the carrier concentration and increasing carrier mobility. Similarly, Jagadish et al. [52] reported a simultaneous increase in the electrical conductivity and Seebeck coefficient by incorporating graphene flakes into recycled carbon fiber (RCF)-Bi_2S_3 composite. The addition of graphene decreases the carrier concentration and introduces interfaces where low-energy carriers were filtered. As a consequence, both Seebeck coefficient and carrier mobility were enhanced and the calculated power factor increases from 0.094 $\mu wm^{-1}k^{-2}$ to 1.53 $\mu wm^{-1}k^{-2}$.

TEM analysis was performed to shed light on the relationship between carrier concentration and carrier mobility and the consequence of electrical behavior enhancement in GNP-2 h and GNP-12 h samples compared with the GNP-1 m sample. Fig. 6 shows a bright-field image of the GNP-1 m sample along with the SAED patterns from two selected areas. The agglomeration of GNP was obvious in the examined samples, which confirms the findings from XRD, Raman spectroscopy, and SEM (see Figs. 1, 3, 4). However, the SAED pattern of the two selected areas exhibits multiple close spots that form an almost full ring and is attributed to the highly crystalline structure of multiple layers of randomly stacked graphene [53–55]. Although graphene maintained its structure and

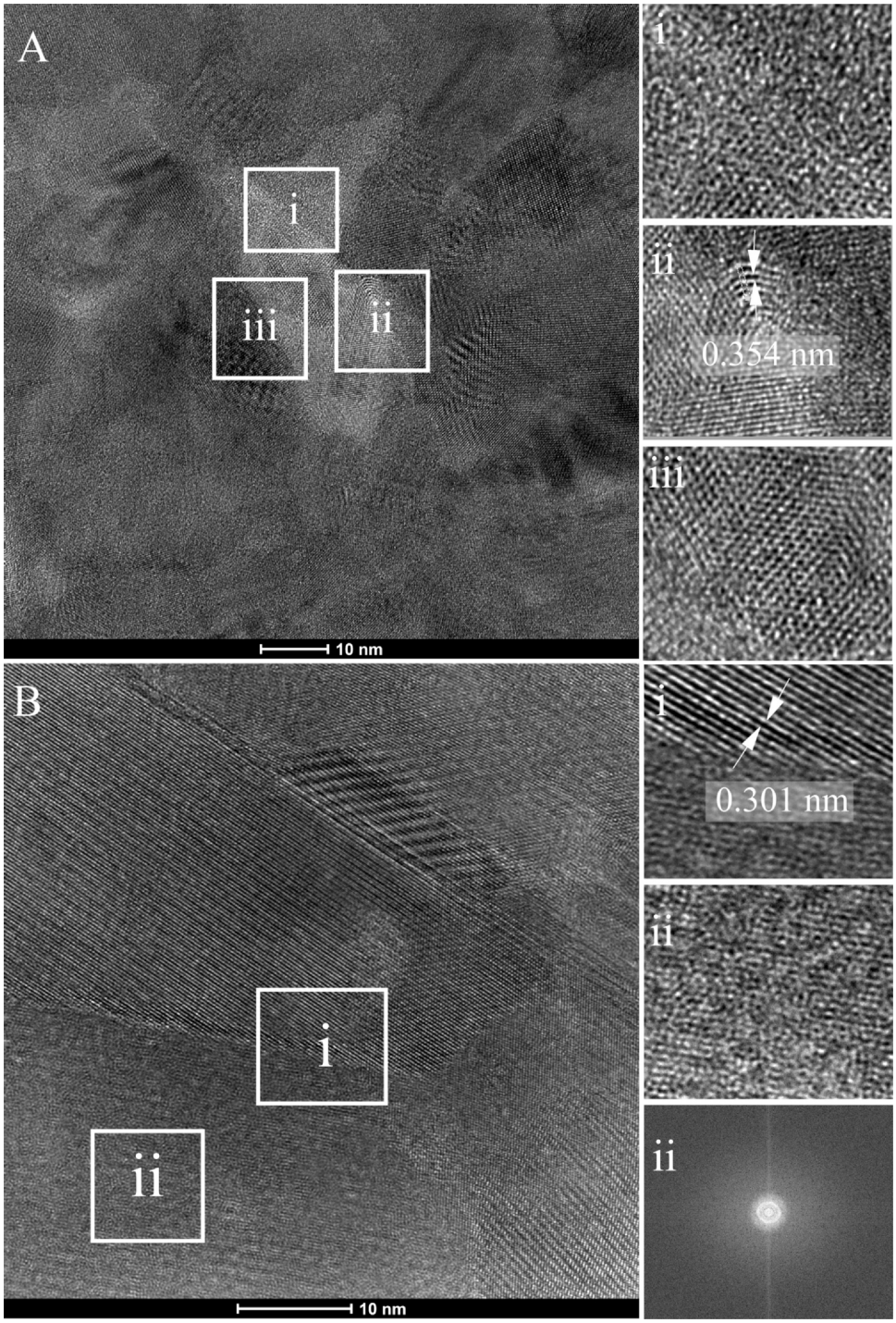

Fig. 7. (A) High-resolution TEM images from the GNP-2 h sample showing different graphene structures: (i) a specified region that represents the amorphous carbon, (ii) a specified region showing the bent area of a morphed graphene structure with d-spacing of 0.354 nm, (iii) a specified area with a hexagonal pattern representing graphene with graphene. (B) A high-resolution TEM image for the GNP-12 h sample with (i) a magnified image of the selected area with d-spacing of 0.301 nm corresponding to (011) planes in the nanostructured SnSe. It represents the coherent and continuous interface between SnSe and graphene, (ii) a magnified area representing an amorphous structure of graphene embedded in the sample beside SnSe with its corresponding FFT.

crystallinity during short milling times, 1 min of milling time was not enough to exfoliate graphene and distribute it homogeneously in the matrix. As a result, the sample demonstrates low electrical properties and extra scattering of carriers, hence reducing carrier concentration and carrier mobility (see Fig. 5B and D) [15,48]. In contrast, several high-degree deformations in the graphene structure have been observed in the GNP-2 h and GNP-12 h samples. Fig. 7 shows high-resolution TEM images of the GNP-2 h and GNP-12 h samples with the corresponding Fast Fourier Transform (FFT) images from selected areas. In Fig. 7A, it can be seen that multiple structures of graphene exist within the sample, including (i) amorphous carbon; (ii) a deformed bent area with interplanar (d) spacing distance of 0.354 nm, representing morphed graphene structure; and (iii) graphene represented by a hexagonal pattern [56]. Morphed graphene is produced by mechanical milling [57]. The formation mechanism of the morphed graphene is suggested to

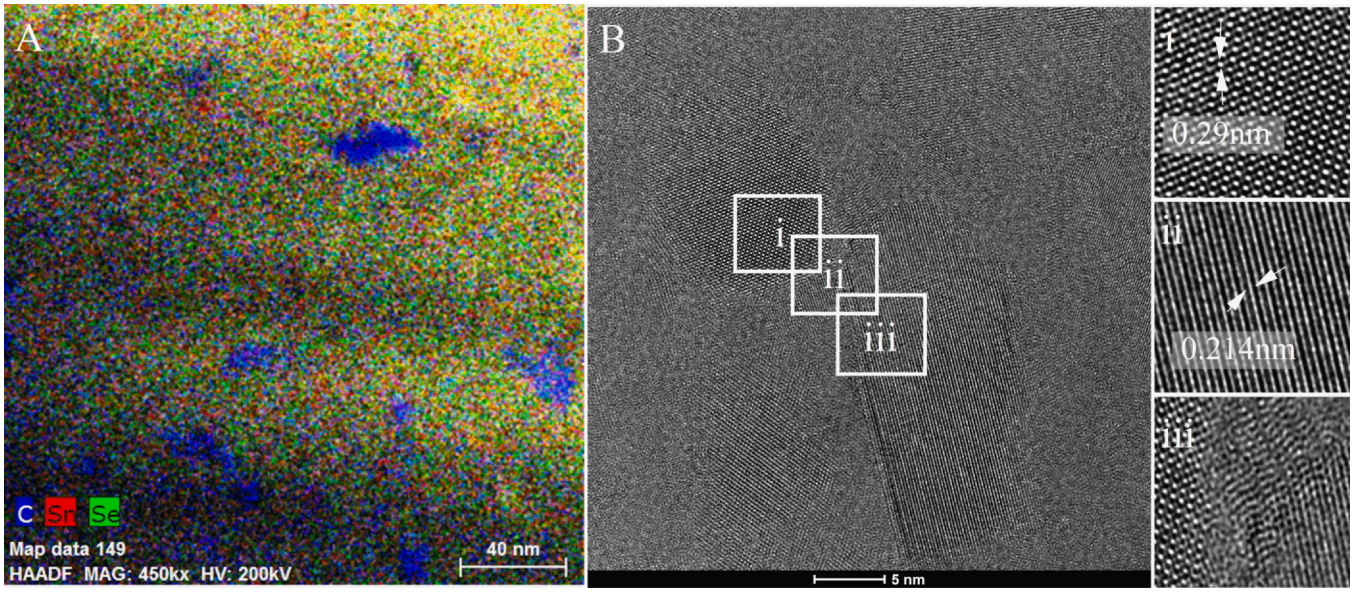

Fig. 8. (A) HAADF elemental map data image of the GNP-2 h sample showing the elemental distribution of Sn, Se, and graphene, where graphene is homogeneously distributed with a certain aggregation along the grain boundaries. (B) High-resolution TEM image of the GNP-2 h sample representing the presence of graphene at the grain boundaries between two tin selenide grains with three selected magnified areas, (i) a SnSe layered structure with d spacing of 0.29 representing (400) planes, (ii) SnSe planes with d spacing of 0.214 nm representing (411) planes, and (iii) an area between the two grains showing a deformed graphene structure settling at the grain boundaries.

nucleate out of a bent area, as shown in Fig. 7. The specific structure is formed as a result of the transformation of sp^2 carbon nature bonding into sp^3, which increases up to the maximum limit and then decreases due to excessive damage and breakage in the crystal [56,58]. Further deformation of graphene structure is detected in the GNP-12 h sample. Fig. 7B represents a high-resolution TEM image of the GNP-12 h. Two distinguished phases of the SnSe with a d-spacing of 0.301 nm correspond to the (011) atomic plane and the graphene with a highly deformed structure. The presence of several deformed graphene structures in the GNP-2 h and GNP-12 h samples is in agreement with the Raman data and confirms the role of milling time in producing an excessive amount of disorders in graphene. This could explain the decrease in carrier concentration with milling time, which was lowest in the GNP-12 h sample.

In contrast, the deformation of graphene structures with milling time is accompanied by a high degree of distribution homogeneity. Fig. 8A shows HAADF elemental mapping of the GNP-2 h sample. It can be seen that graphene is dispersed homogeneously within the matrix with an obvious aggregation along the grain boundaries. Fig. 8B shows a high-resolution TEM image of the GNP-2 h sample, in which graphene appears to be located at the grain boundaries and fills the gap between two distinguished grains of tin selenide. Similar homogeneous distribution with extra fracturing and less aggregation appeared in the HAADF image of the GNP-12 h sample as presented in Fig. 9. The enhanced distribution of graphene in this sample results in increased interfaces, which could explain the obtained maximum Seebeck coefficient (see Fig. 5). The high-resolution TEM images in Figs. 8 and 9 show that the interfaces between the SnSe and graphene in look coherent and continuous, which could facilitate carrier movement between the graphene and SnSe phases and enhance the electrical properties (Fig. 5). The homogeneous distribution of graphene, its preferred dispersion location along the grain boundaries, and the formation of coherent interfaces with the matrix are all factors that could enhance carrier mobility by providing a path for carrier transport and preventing high-energy carriers from being trapped at the grain boundaries [17,19] thereby enhancing the carrier mobility.

4. Conclusion

Tin selenide matrix composites embedded with graphene nanoplatelets were successfully prepared via the mechanical milling method combined with hot pressing. Graphene was added to the matrix at different ball milling times. The short milling time was not enough to exfoliate and disperse graphene in the matrix, which resulted in an agglomeration of graphene and lower electrical transport properties. According to Raman spectroscopy, SEM images, and TEM analysis, milling had a significant effect in deforming the graphene sheets and introducing many defects into their structure. However, a long milling time of up to 12 h effectively dispersed the graphene homogeneously into a SnSe matrix, which provided a bath for carriers to transport. This process enhanced the electrical conductivity by increasing carrier mobility and producing interfaces within the matrix that could filter the low-energy carriers, thus enhancing the Seebeck coefficient. A maximum PF was achieved when graphene was added at the last 2 h of milling at (773 K), whereas the Gr-12 h sample showed the best PF in a wider temperature range (from room temperature up to 720 K). These results demonstrate that mechanical milling is a good preparation method for SnSe/GNPs composite, and increasing the milling time of graphene enhanced the electrical conductivity and the Seebeck coefficient.

CRediT authorship contribution statement

Manal. M. Alsalama: Conceptualization; Data curation; Formal analysis; Investigation; Methodology; Validation; Visualization; Writing - original draft. **Hicham Hamoudi:** Project administration; Supervision. **Khaled M. Youssef:** Conceptualization; Methodology; Funding acquisition; Project. administration; Supervision; Writing - review & editing.

Declaration of Competing Interest

The authors declare that they have no known competing financial interests or personal relationships that could have appeared to influence the work reported in this paper.

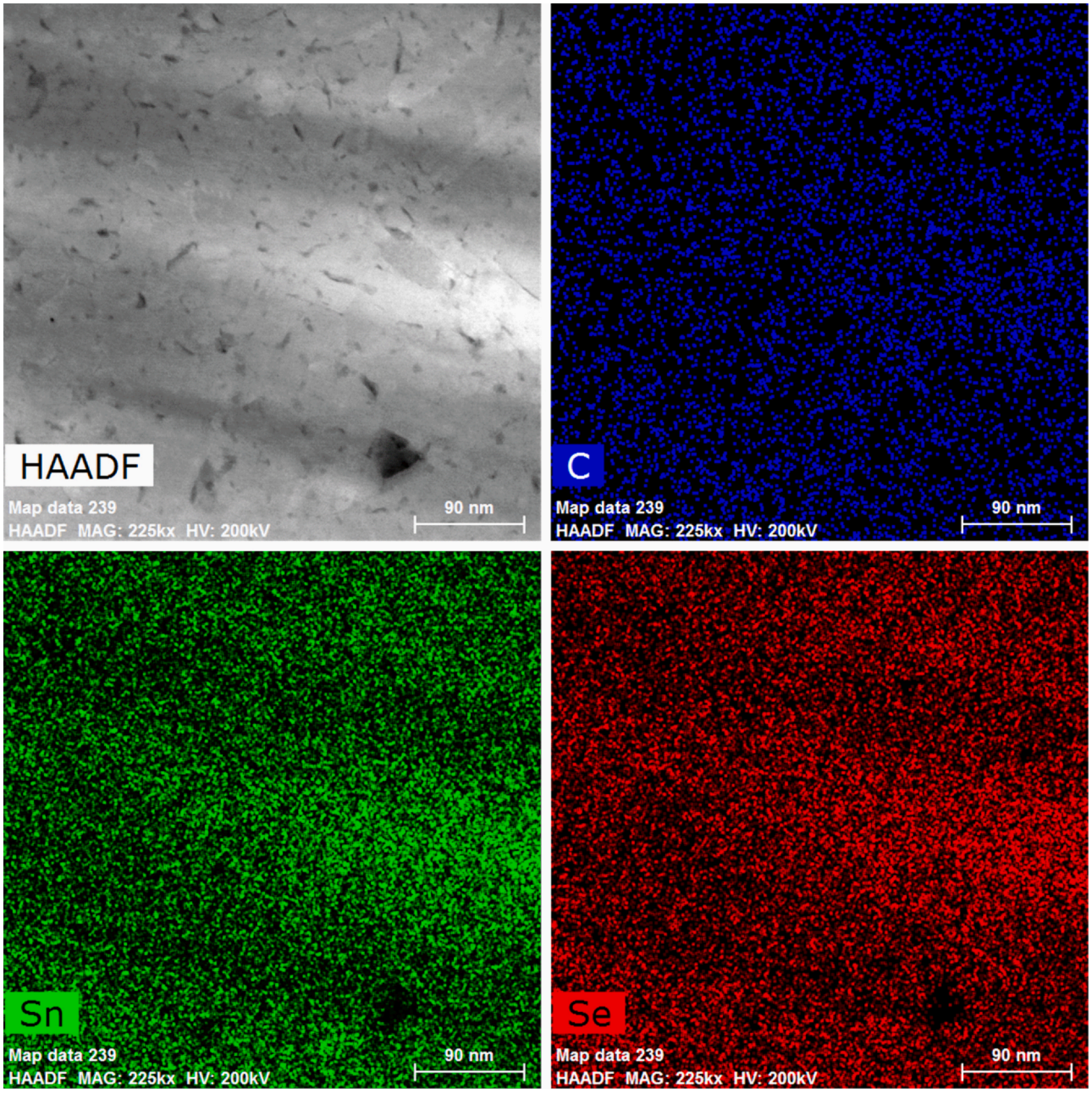

Fig. 9. HAADF image of the GNP-12 h sample with energy-dispersive X-ray spectroscopy mapping analysis of graphene, Sn, and Se showing the uniform distribution of graphene in the sample.

Acknowledgments

This work was made possible by the Qatar Research Leadership program (QRLP) which is under Qatar National Research Fund (QNRF) (a member of the Qatar Foundation) under Grant no. QRLP9-G-3330017, and is supported by the NPRP under Grant no. NPRP10-0206-170366. Open Access funding provided by the Qatar National Library. The statements made herein are solely the responsibility of the authors. The authors would like to acknowledge the the technical assistance provided by Dr. Atif Zekri, Dr. Ayman Samara and Mr. Omar Alhassan at the Imaging and Characterization CORE Labs-Hamad Bin Khalifa University and technical support provided by the Central Laboratory Unit (CLU) and the Center of Advanced Materials (CAM) at Qatar University.

References

[1] L.-D. Zhao, S.H. Lo, Y. Zhang, H. Sun, G. Tan, C. Uher, C. Wolverton, V.P. Dravid, M.G. Kanatzidis, Ultralow thermal conductivity and high thermoelectric figure of merit in SnSe crystals, Nature 508 (7496) (2014) 373–377.
[2] L. Huang, J. Lu, D. Ma, C. Ma, B. Zhang, H. Wang, G. Wang, D.H. Gregory, X. Zhou, G. Han, Facile in situ solution synthesis of SnSe/rGO nanocomposites with enhanced thermoelectric performance, J. Mater. Chem. A 8 (3) (2020) 1394–1402.
[3] X. Wang, et al., Graphene inclusion induced ultralow thermal conductivity and improved figure of merit in p-type SnSe, Nanoscale (2020).
[4] S. Sassi, C. Candolfi, J.B. Vaney, V. Ohorodniichuk, P. Masschelein, A. Dauscher, B. Lenoir, Assessment of the thermoelectric performance of polycrystalline p-type SnSe, Appl. Phys. Lett. 104 (21) (2014) 212105.
[5] B. Asfandiyar, B. Cai, H.L. Zhuang, H. Tang, J.F. Li, Polycrystalline SnSe–Sn1–vS solid solutions: vacancy engineering and nanostructuring leading to high thermoelectric performance, Nano Energy 69 (2020) 104393.

[6] W. Wang, Z. Zheng, F. Li, C. Li, P. Fan, J. Luo, B. Li, Synthesis process and thermoelectric properties of n-type tin selenide thin films, J. Alloy. Compd. 763 (2018) 960–965.
[7] J.A. Hernandez, A. Ruiz, L.F. Fonseca, M.T. Pettes, M. Jose-Yacaman, A. Benitez, Thermoelectric properties of SnSe nanowires with different diameters, Sci. Rep. 8 (1) (2018) 1–8.
[8] C.-L. Chen, H. Wang, Y.Y. Chen, T. Day, G.J. Snyder, Thermoelectric properties of p-type polycrystalline SnSe doped with Ag, J. Mater. Chem. A 2 (29) (2014) 11171–11176.
[9] J.C. Li, D. Li, X.Y. Qin, J. Zhang, Enhanced thermoelectric performance of p-type SnSe doped with Zn, Scr. Mater. 126 (2017) 6–10.
[10] H. Ju, J. Kim, Effect of SiC ceramics on thermoelectric properties of SiC/SnSe composites for solid-state thermoelectric applications, Ceram. Int. 42 (8) (2016) 9550–9556.
[11] D. Li, J.C. Li, X.Y. Qin, J. Zhang, H.X. Xin, C.J. Song, L. Wang, Enhanced thermoelectric performance in SnSe based composites with PbTe nanoinclusions, Energy 116 (2016) 861–866.
[12] J.C. Li, D. Li, W. Xu, X.Y. Qin, Y.Y. Li, J. Zhang, Enhanced thermoelectric performance of SnSe based composites with carbon black nanoinclusions, Appl. Phys. Lett. 109 (17) (2016) 173902.
[13] H. Guo, H. Xin, X. Qin, J. Zhang, D. Li, Y. Li, C. Song, C. Li, Enhanced thermoelectric performance of highly oriented polycrystalline SnSe based composites incorporated with SnTe nanoinclusions, J. Alloy. Compd. 689 (2016) 87–93.
[14] H. Xinmin, et al., Applications of graphene in composite thermoelectric materials, Prog. Chem. 30 (4) (2018) 439.
[15] K. Ahmad, C. Wan, M.A. Al-Eshaikh, A.N. Kadachi, Enhanced thermoelectric performance of Bi2Te3 based graphene nanocomposites, Appl. Surf. Sci. 474 (2019) 2–8.
[16] D. Suh, S. Lee, H. Mun, S.H. Park, K.H. Lee, S. Wng Kim, J.Y. Choi, S. Baik, Enhanced thermoelectric performance of Bi0. 5Sb1. 5Te3-expanded graphene composites by simultaneous modulation of electronic and thermal carrier transport, Nano Energy 13 (2015) 67–76.
[17] D. Zhao, X. Wang, D. Wu, Enhanced thermoelectric properties of graphene/Cu2SnSe3 composites, Crystals 7 (3) (2017) 71.
[18] K. Agarwal, V. Kaushik, D. Varandani, A. Dhar, B.R. Mehta, Nanoscale thermoelectric properties of Bi2Te3–Graphene nanocomposites: conducting atomic force, scanning thermal and kelvin probe microscopy studies, J. Alloy. Compd. 681 (2016) 394–401.
[19] K. Ahmad, C. Wan, P.-A. Zong, Thermoelectric properties of BiSbTe/graphene nanocomposites, J. Mater. Sci. Mater. Electron. 30 (13) (2019) 11923–11930.
[20] W.H. Shin, K. Ahn, M. Jeong, J.S. Yoon, J.M. Song, S. Lee, W.S. Seo, Y.S. Lim, Enhanced thermoelectric performance of reduced graphene oxide incorporated bismuth-antimony-telluride by lattice thermal conductivity reduction, J. Alloy. Compd. 718 (2017) 342–348.
[21] B. Feng, J. Xie, G. Cao, T. Zhu, X. Zhao, Enhanced thermoelectric properties of p-type CoSb 3/graphene nanocomposite, J. Mater. Chem. A 1 (42) (2013) 13111–13119.
[22] H. Ju, J. Kim, Preparation and structure dependent thermoelectric properties of nanostructured bulk bismuth telluride with graphene, J. Alloy. Compd. 664 (2016) 639–647.
[23] J. Dong, W. Liu, H. Li, X. Su, X. Tang, C. Uher, In situ synthesis and thermoelectric properties of PbTe–graphene nanocomposites by utilizing a facile and novel wet chemical method, J. Mater. Chem. A 1 (40) (2013) 12503–12511.
[24] S. Kumar, M. Faraz, N. Khare, Enhanced thermoelectric properties of Sb2Te3-graphene nanocomposite, Mater. Res. Express 6 (8) (2019) 085079.
[25] S. Kumar, S. Singh, P.K. Dhawan, R.R. Yadav, N. Khare, Effect of graphene nanofillers on the enhanced thermoelectric properties of Bi2Te3 nanosheets: elucidating the role of interface in de-coupling the electrical and thermal characteristics, Nanotechnology 29 (13) (2018) 135703.
[26] N.V. Ponraj, S.C. Vettivel, A. Azhagurajan, X. Sahaya shajan, P.Y. Nabhiraj, T. Theivasanthi, P. Selvakumar, A.H. Lenin, Effect of milling on dispersion of graphene nanosheet reinforcement in different morphology copper powder matrix, Surf. Interfaces 9 (2017) 260–265.
[27] A. Liang, X. Jiang, X. Hong, Y. Jiang, Z. Shao, D. Zhu, Recent developments concerning the dispersion methods and mechanisms of graphene, Coatings 8 (1) (2018) 33.
[28] H. Tang, F.H. Sun, J.F. Dong, Asfandiyar, H.L. Zhuang, Y. Pan, J.F. Li, Graphene network in copper sulfide leading to enhanced thermoelectric properties and thermal stability, Nano Energy 49 (2018) 267–273.
[29] Z. Yu, W. Yang, C. Zhou, N. Zhang, Z. Chao, H. liu, Y. Cao, Y. Sun, P. Shao, G. Wu, Effect of ball milling time on graphene nanosheets reinforced Al6063 composite fabricated by pressure infiltration method, Carbon 141 (2019) 25–39.
[30] K.M. Youssef, R.O. Scattergood, K.L. Murty, C.C. Koch, Nanocrystalline Al–Mg alloy with ultrahigh strength and good ductility, Scr. Mater. 54 (2) (2006) 251–256.
[31] M.S. El-Asfoury, M.N.A. Nasr, K. Nakamura, A. Abdel-Moneim, Thermoelectric power factor performance of Bi85Sb15/graphene composite, Jap. J. Appl. Phys. 55 (4) (2016) 045802.
[32] J. Song, Z. Yu, M.L. Gordin, S. Hu, R. Yi, D. Tang, T. Walter, M. Regula, D. Choi, X. Li, A. Manivannan, D. Wang, Chemically bonded phosphorus/graphene hybrid as a high performance anode for sodium-ion batteries, Nano Lett. 14 (11) (2014) 6329–6335.
[33] M.W. Smith, I. Dallmeyer, T.J. Johnson, C.S. Brauer, J.S. McEwen, J.F. Espinal, M. Garcia-Perez, Structural analysis of char by Raman spectroscopy: improving band assignments through computational calculations from first principles, Carbon 100 (2016) 678–692.
[34] H.D. Le, et al., Synthesis of multi-layer graphene films on copper tape by atmospheric pressure chemical vapor deposition method, Adv. Nat. Sci. Nanosci. Nanotechnol. 4 (3) (2013) 035012.
[35] M. Hiramatsu, H. Kondo, M. Hori, Graphene nanowalls, New Progress on Graphene Research, (2013), pp. 235–260.
[36] C. Nath, C.Y. Chueh, Y.K. Kuo, J.P. Singh, Thermoelectric properties of p-type SrTiO3/graphene layers nanohybrids, J. Appl. Phys. 125 (18) (2019) 185101.
[37] I. Estrada-Guel, F. Robles-Hernandez, R. Martínez-Sánchez, A green method for graphite exfoliation Using a mechanochemical route, Materials Characterization, Springer, 2015, pp. 179–188.
[38] G. Gao, D. Liu, S. Tang, C. Huang, M. He, Y. Guo, X. Sun, B. Gao, Heat-initiated chemical functionalization of graphene, Sci. Rep. 6 (2016) 20034.
[39] A. Najimi, H. Shahverdi, Effect of milling methods on microstructures and mechanical properties of Al6061-CNT composite fabricated by spark plasma sintering, Mater. Sci. Eng. A 702 (2017) 87–95.
[40] M. Li, H. Gao, J. Liang, S. Gu, W. You, D. Shu, J. Wang, B. Sun, Microstructure evolution and properties of graphene nanoplatelets reinforced aluminum matrix composites, Mater. Charact. 140 (2018) 172–178.
[41] T. Lee, F.A. Mas'ud, M.J. Kim, H. Rho, Spatially resolved Raman spectroscopy of defects, strains, and strain fluctuations in domain structures of monolayer graphene, Sci. Rep. 7 (1) (2017) 1–8.
[42] Y. Cui, L. Wang, B. Li, G. Cao, W. Fei, Effect of ball milling on the defeat of few-layer graphene and properties of copper matrix composites, Acta Metall. Sin. (Engl. Lett.) 27 (5) (2014) 937–943.
[43] M. Bastwros, G.Y. Kim, C. Zhu, K. Zhang, S. Wang, X. Tang, X. Wang, Effect of ball milling on graphene reinforced Al6061 composite fabricated by semi-solid sintering, Compos. Part B Eng. 60 (2014) 111–118.
[44] A.-S. Al-Sherbini, M. Bakr, I. Ghoneim, M. Saad, Exfoliation of graphene sheets via high energy wet milling of graphite in 2-ethylhexanol and kerosene, J. Adv. Res. 8 (3) (2017) 209–215.
[45] C. Li, X. Qin, Y. Li, D. Li, J. Zhang, H. Guo, H. Xin, C. Song, Simultaneous increase in conductivity and phonon scattering in a graphene nanosheets/(Bi2Te3) 0.2 (Sb2Te3) 0.8 thermoelectric nanocomposite, J. Alloy. Compd. 661 (2016) 389–395.
[46] J. Zhang, D. Wu, D. He, D. Feng, M. Yin, X. Qin, J. He, Extraordinary thermoelectric performance realized in n-type PbTe through multiphase nanostructure engineering, Adv. Mater. 29 (39) (2017) 1703148.
[47] H. Ju, J. Kim, The effect of temperature on thermoelectric properties of n-type Bi 2 Te 3 nanowire/graphene layer-by-layer hybrid composites, Dalton Trans. 44 (26) (2015) 11755–11762.
[48] M.S. El-Asfoury, M.N.A. Nasr, K. Nakamura, A. Abdel-Moneim, Enhanced thermoelectric performance of Bi85Sb15-graphene composite by modulation carrier transport and density of state effective mass, J. Alloy. Compd. 745 (2018) 331–340.
[49] C. Gayner, Y. Amouyal, Energy filtering of charge carriers: current trends, challenges, and prospects for thermoelectric materials, Adv. Funct. Mater. 30 (18) (2020) 1901789.
[50] H. Chen, C. Yang, H. Liu, G. Zhang, D. Wan, F. Huang, Thermoelectric properties of CuInTe 2/graphene composites, CrystEngComm 15 (34) (2013) 6648–6651.
[51] M. Li, D.L. Cortie, J. Liu, D. Yu, S.M.K.N. Islam, L. Zhao, D.R.G. Mitchell, R.A. Mole, M.B. Cortie, S. Dou, X. Wang, Ultra-high thermoelectric performance in graphene incorporated Cu2Se: Role of mismatching phonon modes, Nano Energy 53 (2018) 993–1002.
[52] P.R. Jagadish, et al., Effect of graphene doping on the charge carrier and thermoelectric properties of RCF-Bi2S3 composites, AIP Conference Proceedings, AIP Publishing LLC, 2019.
[53] J. Sengupta, K. Das, U.N. Nandi, C. Jacob, Substrate free synthesis of graphene nanoflakes by atmospheric pressure chemical vapour deposition using Ni powder as a catalyst, Bull. Mater. Sci. 42 (4) (2019) 136.
[54] T. Cui, R. Lv, Z.H. Huang, H. Zhu, Y. Jia, S. Chen, K. Wang, D. Wu, F. Kang, Low-temperature synthesis of multilayer graphene/amorphous carbon hybrid films and their potential application in solar cells, Nanoscale Res. Lett. 7 (1) (2012) 1–7.
[55] R. Zan, Q. M, R. Jalil, U. Bangert, Atomic structure of graphene and h-BN layers and their interactions with metals, Advances in Graphene Science, IntechOpen, 2013.
[56] H.A. Calderon, F. Alvarez Ramirez, D. Barber, V.G. Hadjiev, A. Okonkwo, R. Ordoñez Olivares, I. Estrada Guel, F.C. Robles Hernandez, Enhanced elastic behavior of all-carbon composites reinforced by in-situ synthesized morphed graphene, Carbon 153 (2019) 657–662.
[57] H.A. Calderon, I. Estrada-Guel, F. Alvarez-Ramírez, V.G. Hadjiev, F.C. Robles Hernandez, Morphed graphene nanostructures: experimental evidence for existence, Carbon 102 (2016) 288–296.
[58] H. Calderon, et al., HRTEM low dose: the unfold of the morphed graphene, from amorphous carbon to morphed graphenes, Adv. Struct. Chem. Imaging (2017) 2.